Melting kinetics, ultra-drawability and microstructure of nascent ultra-high molecular weight polyethylene powder

Author(s):
Christakopoulos, Fotis; Troisi, Enrico M.; Sologubenko, Alla; Friederichs, Nic; Stricker, Laura; Tervoort, Theo A.

Publication date:
2021-04-22

Permanent link:
https://doi.org/10.3929/ethz-b-000477043

Originally published in:
Polymer 222, https://doi.org/10.1016/j.polymer.2021.123633

Polymer 222 (2021) 123633

Contents lists available at ScienceDirect

Polymer

journal homepage: http://www.elsevier.com/locate/polymer

Melting kinetics, ultra-drawability and microstructure of nascent ultra-high molecular weight polyethylene powder

Fotis Christakopoulos [a], Enrico M. Troisi [b], Alla S. Sologubenko [c], Nic Friederichs [b], Laura Stricker [a], Theo A. Tervoort [a,*]

[a] Soft Materials, Department of Materials, ETH Zürich, 8093, Zurich, Switzerland
[b] SABIC Technology and Innovation, 6160AH, Geleen, the Netherlands
[c] ScopeM, Scientific Center for Optical and Electron Microscopy, ETH Zürich, 8093, Zurich, Switzerland

ARTICLE INFO

Keywords:
Nascent UHMWPE
Melting kinetics
Isoconversional analysis
Ultra-drawing
Lamellar thickness
Differential Scanning Calorimetry (DSC)
Scanning Transmission Electron Microscopy (STEM)

ABSTRACT

For the production of high-performance polyethylene fibers and tapes by ultra drawing, using solid-state processing of disentangled nascent ultra-high molecular weight polyethylene (UHMWPE), the maximum draw ratio is an important design parameter, as it determines the maximum degree of chain alignment and, therewith, the properties of the final product. It would, therefore, be advantageous to have a fast scanning method to estimate the maximum drawability of reactor powders. In the present work, the melting behavior of nascent UHMWPE reactor powder was studied by differential scanning calorimetry, followed by isoconversional analysis to evaluate the apparent activation energy barrier of melting for the different UHMWPE grades of different level of disentanglement. Powder samples were solid-sate processed into tapes at elevated temperature. Ultra drawing of these tapes at the optimum drawing temperature allowed for the evaluation of the maximum draw ratio (λ_{max}) that is determined by the entanglement density. The morphology of the lamellar structure of the nascent powder was studied by small-angle X-ray scattering and by scanning transmission electron microscopy analyses. A correlation between the melting kinetics, the microstructure and the maximum draw ratio was observed for all grades, suggesting that the apparent activation energy of melting can be used as a screening method to estimate the maximum draw ratio.

1. Introduction

Polymeric materials often represent an attractive compromise between the properties of the final product and ease of processing. This is especially true for polymeric fibers. For example, relatively low-viscous polyesters and polyamides allow for high-speed melt-spinning, with wind-up velocities in excess of 5 km min^{-1} [1]. This allows for mass-production of fiber material, albeit with modest mechanical properties that are only sufficient for relatively low-demanding applications, such as tapestry and clothing [2]. In contrast, high-performance fibers consisting of stiff (lyotropic) polymer systems or flexible polymers of ultra-high molar mass, hold the promise of superior mechanical performance due to nearly full orientation of the macromolecular chains [3–5]. However, these superior properties are notoriously difficult to achieve due to the intractable nature of the starting materials. It is, therefore, not surprising that the quest for efficient processing routes to produce high-performance polymer fibers is still an active field of research [6].

In case of state-of-the-art high-performance polyethylene (HPPE) fibers, the close-to-perfect macromolecular alignment that is needed to obtain high stiffness and strength is achieved by large-scale uniaxial solid-state plastic deformation of disentangled ultra-high molecular weight polyethylene (UHMWPE) precursor fibers at elevated temperatures, the so-called "ultra-drawing process" [7]. In "soft" semi-crystalline polymers above the glass-transition temperature, such as polyethylene, where the crystal interactions are dominated by van der Waals bonds, the ultimate solid-state drawability is mostly determined by the entanglement density [8], although crystal perfection might also have an influence [9]. Therefore, to obtain polyethylene fibers with superior mechanical properties, precursor fibers are needed that have a low entanglement density, allowing for a maximum draw ratio $\lambda_{max} > 30$, where λ_{max} is defined as the ratio of final to initial length.

The reduction of entanglement density that is needed to allow for large plastic deformation is typically achieved by crystallization of the

* Corresponding author.
E-mail address: tervoort@ethz.ch (T.A. Tervoort).

https://doi.org/10.1016/j.polymer.2021.123633
Received 8 January 2021; Received in revised form 12 February 2021; Accepted 8 March 2021
Available online 13 March 2021

Table 1
Abbreviated names, molecular weight and melting peak temperature of the UHMWPE grades used.

Grade	Abbreviated name	M_v (kg mol^{-1})	T_m (°C)
Commercial GUR 4120	GUR	5000	139.8
Ziegler-Natta entangled	ZNE	8000	140.9
Ziegler-Natta low entangled	ZNLE	4500	140.0
Single-site catalyst A	SSCA	5500	140.3
Single-site catalyst B	SSCB	5000	140.7

UHMWPE from dilute solution, leading to the so-called "gel-spinning process" [7,10]. However, this leads to an unfavorable processing method involving large amounts of flammable and poisonous solvents such as decalin. One recently proposed alternative is the use of green solvents, such as vegetable oils and stearic acid [9,11]. Another method was proposed by Smith et al. [12] and involves the direct synthesis of disentangled UHMWPE reactor powder [13–15]. This special, nascent (also called "virgin"), morphology can be achieved by polymerization at relatively mild conditions or by having catalytic centers apart from each other, as for example by using single-site catalysts [16–18]. In both cases, the as-polymerized polymer chain is thought to crystallize before the formation of intermolecular entanglements can occur, resulting in a UHMWPE reactor powder with reduced entanglement density.

In case of solution crystallization, control over the maximum drawability is achieved by adjusting the entanglement density through the UHMWPE solution concentration [8] and, additionally, by solvent quality [9,11]. In contrast, the entanglement density of nascent UHMWPE reactor powder is more difficult to control or even determine. However, it was observed that nascent UHMWPE powders depict pronounced superheating during melting that is related to the entanglement density and, thereby, to the ultimate draw ratio [19–22]. In these studies, it was shown that the time constant for melting was lower for disentangled materials, in other words, that disentangled nascent powders melt "faster".

A standard tool for quantitative analysis of thermally activated processes, which is recommended by the Kinetics Committee of the International Confederation for Thermal Analysis and Calorimetry, is the isoconversional method [23,24]. The isoconversional analysis allows for a reliable way of evaluating a calorimetric dataset, without assuming any particular reaction model beforehand and has been utilized for the investigation of melting kinetics of polymers in numerous studies [24–32].

It is, therefore, the objective of this study to apply the isoconversional method to determine the melting kinetics of various nascent UHMWPE samples of approximately equal molecular weight, but with different entanglement densities, resulting in different maximum draw ratios. In addition, for all samples, an important morphological characteristic, the lamellar thickness, will be measured. Finally, we will attempt to correlate the maximum draw ratio to the apparent activation energy for melting and the lamellar thickness.

2. Experimental

2.1. Materials

Different grades of nascent UHMWPE reactor powder were used. Those include a commercial UHMWPE grade, namely GUR4120 supplied from Ticona. The rest of the samples were kindly provided by SABIC and were produced using different catalytic systems and under different polymerization conditions. They consisted of two UHMWPE grades produced by a Ziegler-Natta catalyst, an entangled and a low entangled, and two highly disentangled UHMWPE grades, synthesized using different single-site catalytic systems. As the materials are produced through different catalytic systems and polymerization conditions they are expected to have a different degree of disentanglement. The abbreviated names that are used in the article for each grade, together with the viscosity average molar mass, M_v, as measured from the intrinsic viscosity with the Mark-Houwnik equation and the melting peak temperature, as measured by DSC at a heating rate of 10 °C min^{-1}, are presented in Table 1.

2.2. Solid-state drawability experiments

For the preparation of solid-state drawability specimen, 2 g of UHMWPE reactor powder was compression molded at 200 bar and 120 °C, below the melting temperature, for 20 min into 1 mm thick films. The films were then drawn in the solid state in a two-step process. First, to a draw ratio (λ) of about 3.5 by calendering, using a Collin W100T calendering machine, at 125 °C. Second, dumbbell-shaped samples, according to ISO 527-2 type 5B, were cut from the calendered films and drawn in an Instron 5864 static mechanical tester, equipped with an environment-control chamber, at 120 °C at an initial strain rate of 0.1 s^{-1}, until failure occurred. The draw ratio is calculated from the displacement of the cross-head and is the mean value of at least five measurements. The maximum draw ratio (λ_{max}) of each sample corresponds to the product of the two drawing steps.

2.3. Thermal analysis

For the thermal analysis, DSC experiments were conducted with a heat flux Mettler-Toledo 822e. Indium and Zinc standards were used to perform automated temperature, heat flow and tau-lag calibrations. The tau-lag calibration consists of two compensations, matching the program temperature to the reference temperature, and adjusting for the heating rate as described by the equation $\Delta T_{lag} = q\tau_{lag}$, where q is the heating rate, ΔT_{lag} is the difference between the furnace and reference temperatures and τ_{lag} is the adjustment factor [33]. The specific value of the tau-lag adjustment is calculated from multiple heating rates, between 1 °C min^{-1} and 10 °C min^{-1}. DSC thermographs were recorded under N_2 flow of 20 L min^{-1} with a sample weight of 2 mg($\pm$ 50 μg). A value of 293 J g^{-1} was used for the heat of fusion of polyethylene [34]. The software packages Matlab and Igor Pro were employed to perform all numerical fits and analyses.

2.4. Isoconversional analysis

Isoconversional analysis is focused on evaluating reactions at the same extent of conversion (α), obtained through different temperature protocols. That is achieved in a model-free way, without assuming a reaction model beforehand [24,35–37]. In the case of melting of polymers, investigated by DSC, this can be achieved in two ways. The first consists of isothermal experiments. Another way is by conducting, non-isothermal, constant heating rate experiments with a different heating program (heating rate, β) between each experiment. Due to the inaccuracy of the isothermal experiments regarding the amount of material that is molten during the heating to the isothermal temperature and the long times needed for those experiments, the non-isothermal experiments were conducted. In general, isoconversional kinetic analysis involves evaluating a dependence of the apparent activation energy E_α on conversion or temperature and using this dependence to predict and explore the mechanisms of thermally stimulated processes [23]. The general form of the basic rate equation for a thermally stimulated process can be written as:

$$\left(\frac{d\alpha}{dt}\right) = k(T,\alpha)f(\alpha) \quad (1)$$

where α is the extent of melting ("conversion"), which runs from 0 (fully crystalline) to 1 (fully molten), t the time, T the temperature, $f(\alpha)$ the mathematical function that represents the reaction mechanism and $k(T)$ the rate coefficient [38]. The dependence of the rate coefficient on

temperature is typically given by an Arrhenius law [39]:

$$k(T,\alpha) = A(\alpha)e^{-E(\alpha)/RT} \tag{2}$$

Here, E is the activation energy, A the pre-exponential factor and R the universal gas constant. The isoconversional principle states, that at a constant extent of conversion, the reaction rate is only a function of temperature [29], and so according to Eq. (1)

$$\left[\frac{\partial \ln(d\alpha/dt)}{\partial T^{-1}}\right]_\alpha = \left[\frac{\partial \ln k}{\partial T^{-1}}\right]_\alpha + \left[\frac{\partial \ln f(\alpha)}{\partial T^{-1}}\right]_\alpha \tag{3}$$

The subscript α indicates values related to a certain extent of conversion. Following the isoconversional principle, $f(\alpha)$ does not depend on temperature when α is constant, therefore:

$$\left[\frac{\partial \ln(d\alpha/dt)}{\partial T^{-1}}\right]_\alpha = -E_\alpha \Big/ R \tag{4}$$

Using Eq. (4), a model-free value of the apparent activation energy (E_α) is estimated for each degree of conversion. Depending on the nature of the experimental data, a differential or integral isoconversional method can be used. As the current data originates from DSC measurements and so the data is already in differential form, the differential isoconversional method of Friedman has been employed [36]. Application of this method requires knowledge of the reaction rate $(d\alpha/dt)_{\alpha,i}$ and the temperature $T_{\alpha,i}$ corresponding to a given extent of conversion, for the ith temperature program used. From Eq. (1) and Eq. (2) we get:

$$d\alpha / dt = A(\alpha)f(\alpha)\exp(-E(\alpha) / RT) \tag{5}$$

and by using the isoconversional method at a constant extent of conversion, α:

$$\ln(d\alpha/dt)_{\alpha,i} = \ln[A_\alpha f(\alpha)] - E_\alpha \Big/ RT_{\alpha,i} \tag{6}$$

where $\ln[A_\alpha f(\alpha)]$ is constant. The apparent activation energy E_α can be determined by a plot of the left hand side of Eq. (6) against the reciprocal absolute temperature for each extent of conversion for every heating program. E_α is calculated from the slope of the resulting Arrhenius-like plots.

The melting runs were conducted in the temperature range of 20–180 °C using $i = 19$ different heating rates, from 1 °C min^{-1} to 10 °C min^{-1} with steps of 0.5 °C min^{-1}, that fall within the range of the tau-lag calibration. For each heating run a new sample was used, as the melting behavior of the nascent reactor powder is under investigation. Two replications were conducted for each heating rate and all are included in the analysis, in order to improve accuracy.

2.5. Wide- and small-angle X-ray scattering

Wide-angle X-ray scattering measurements were performed on a Panalytical Xpert-Pro equipped with a Cu anode and a Bragg-Brentano geometry, using Cu $K_{\alpha 1}$ wavelength of 1.540598 Å, a scan range of 2θ from 3 ° to 80 °, and a scan-step size of 0.00167 °. Crystallinity was measured from the ratio of the crystalline peaks of 110 and 200 spacings to the total intensity of the crystalline and the amorphous part, following the internal comparison method of Ruland and using the correction factors for polyethylene from Mo et al., [40,41].

For the small-angle X-ray scattering the samples were prepared according to the protocol of Westfahl and Cardoso [42]. Namely, the nascent powder was dried overnight in a vacuum oven at 60 °C and then infiltrated by a contrast fluid mixture of 0.67 toluene and 0.33 chloroform, by molar fraction, under vacuum in a Schlenk tube. The measurements were conducted on a Panalytical Empyrean series 2 with Cu $K\alpha 1$ wavelength of 1.540598 Å. Equipped with a PIXcel1D detector and with a scan range of 2θ from 0.04 ° to 2.11 °, a scan step size of 0.005 ° and a time per step of 300 s. The scattered intensity was recorded as a function of the scattering vector q, defined as $q = 4\pi/\lambda \ \sin(\theta)$, where 2θ is the angle between the incident beam and the detector, measuring the scattering intensity, and λ is the wavelength of the radiation. The Lorentz-correction was applied and the scattering curves were further corrected for thermal density fluctuations. The latter seemed appropriate for our data due to the presence of the contrast fluid mixture, as even in the blank measurement, of a capillary filled only with the contrast fluid mixture, the scattering intensity was increasing at higher q-values [42]. In principle, thermal density fluctuations due to the contrast fluid alone should be readily corrected after subtraction of the background scattering, however the powder/contrast fluid interface might enhance the effect of these fluctuations. In addition, porosity might play a role if the system is not fully equilibrated (all the pores are filled) during the measurement. For the thermal-density fluctuation correction, Iq^4 was plotted against q^4 for each grade, and the slope of the linear portion was estimated for $q^4 > 1$, to be in the Porod region. The resulting slope was then subtracted from the scattering intensity of the respective grade [43,44]. The average long period L of the lamellar stacking, was determined from the q-value, q_{max}, at which the Lorentz-corrected intensity reached a maximum, using the Bragg's condition: $L = 2\pi/q_{max}$. The lamellar thickness l was calculated by multiplying the long period with the crystal volume fraction [44].

2.6. Electron microscopy

Morphological studies of the nascent UHMWPE powders of different entanglement states were studied by transmission electron microscopy (TEM) using a Thermofischer Scientific Talos F200× instrument operated at 200 kV acceleration voltage in a scanning (STEM) mode. The atomic number sensitive imaging with the high angle annular dark field (HAADF) detector was used for the direct visualization of the, stained by a high atomic number compound, amorphous regions in the specimens. As a result, the measurements of the thickness of crystalline lamellae between the amorphous regions were straightforward and were performed using the ImageJ package for image analyses. The elemental content distribution (chemical mapping) in the specimens was analyzed by spectrum imaging (SI) using energy dispersive spectroscopy (EDS) in the STEM mode with the probe size of about 0.6 nm. For the staining of the TEM specimens, the nascent UHMWPE powder was immersed in a ruthenium tetroxide solution and then embedded in fresh prepared Epon-Araldite resin. Ultra-thin slices were cut with a diamond knife in a Leica FC6 ultramicrotome.

2.7. Fourier analysis of STEM images

Frequency analysis of the STEM images was performed, to detect emerging characteristic length scales due to the presence of repeating patterns, such as those produced by lamellae. In each image, a square region of interest of around 90 nm × 90 nm (512 × 512 pixels), surrounding the area where lamellar structure is visible, was cropped. In order to reduce possible artefacts due to edge effects, windowing by weighting the image with a 2D circular Tukey window H(x,y) was applied [45]:

$$\begin{cases} H(x,y) = 1 & \text{for } r \leqslant \alpha L/2 \\ H(x,y) = \frac{1}{2}\left[1 + \cos\frac{\pi(r - \alpha L/2)}{(1-\alpha)L/2}\right] & \text{for } r \leqslant \alpha L \Big/ 2 < r \leq L \Big/ 2 \\ H(x,y) = 0 & \text{for } r > L/2, \end{cases} \tag{7}$$

where $r = \sqrt{(x - L/2)^2 + (y - L/2)^2}$ corresponds to the radial position of the point (x,y) in respect to the center of the image, L refers to the image size and $\alpha = 0.5$ is a scaling factor. Fast-Fourier transform (FFT) was performed, thus obtaining a representation of the original image in the frequency domain. Then the 2D power spectrum was considered and

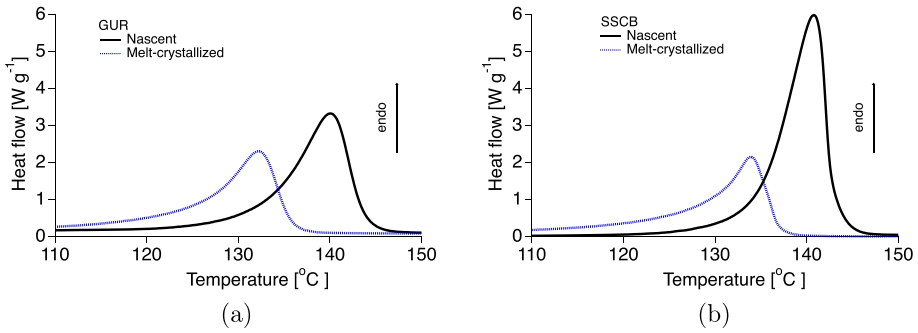

Fig. 1. Differential scanning calorimetry thermographs of the melting of nascent (black solid line) and melt-crystallized (blue dotted line) samples of (a) GUR and (b) SSCB. The difference in the melting peak temperature and enthalpy between the nascent and melt-crystallized material is evident in both cases. (For interpretation of the references to colour in this figure legend, the reader is referred to the web version of this article.)

Table 2
Values of crystal fraction as measured by WAXS, the apparent activation energy at 50%, $E_{0.5}$, lamellar thickness l as measured by STEM using an edge-filter and by Fourier analysis and λ_{max} for the UHMWPE grades examined.

Grade	χ_{WAXS}	$E_{0.5}$	λ_{max}	l (Edge)	l (Fourier)
	(−)	(kJ/mol)	(−)	(nm)	(nm)
GUR	0.63	2252 ± 271	1 ± -	9.68 ± 0.72	10.30 ± 2.08
ZNE	0.59	1978 ± 284	4.5 ± 0.2	7.70 ± 0.49	8.71 ± 1.17
ZNLE	0.70	1506 ± 105	115 ± 9	6.06 ± 0.51	6.10 ± 1.01
SSCA	0.73	1172 ± 105	215 ± 16	3.84 ± 0.30	3.14 ± 0.30
SSCB	0.78	1118 ± 140	240 ± 12	3.77 ± 0.46	2.92 ± 0.27

averaged in the angular direction from 0 to 2π. Hence, the radial profile of the power spectrum was obtained. Such a profile was further smoothed by means of a moving averages procedure over a three-points window. The peaks were detected in the radial profile of the power spectrum, by means of their prominence with respect to the closest minima. After converting from Fourier space to real space, visual inspection of the images was used to verify the correspondence between the peaks position in the power spectrum and the visible repeating features. In particular, it was observed that the peak with the highest prominence corresponds to the long period. Hence, this value was multiplied by the crystal volume fraction to derive the corresponding lamellar thickness. The width of the peaks, measured at the median point of the segment denoting their prominence (height) was used for the calculation of the standard deviation. The aforementioned procedure was performed by means of an in-house code written in ImageJ-macro language, based on the Fiji (ImageJ) native FFT plugin, the H. Glünder's Windowing plugin [46] and Philippe Carl's Radial Profile Extended plugin [47], in combination with an in-house Matlab code.

3. Results and discussion

3.1. Ultra-drawability

Disentangled reactor powders, compacted below the melting temperature, can be drawn to high draw ratios in the solid state [13,14]. The maximum achievable draw ratio (λ_{max}) scales with the amount of entanglements according to Eq. (8), where M_e corresponds to the molecular weight between entanglements, N_e is the number of segments between entanglements, L_0 is the monomer length and c_∞ is the characteristic ratio [8]:

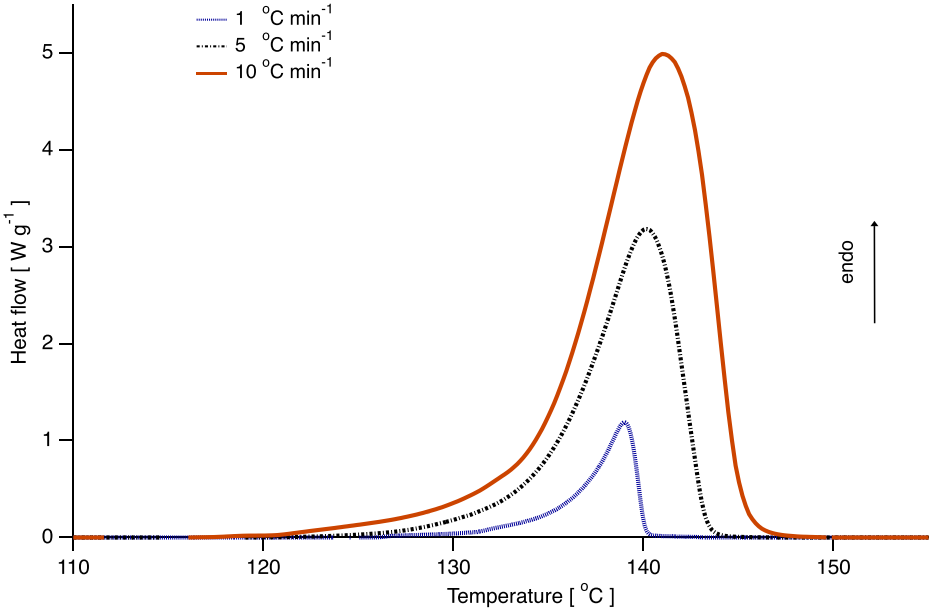

Fig. 2. Differential scanning calorimetry thermograph of the melting of SSCB samples at different heating rates, where the increase in T_m by increasing heating rate can be seen.

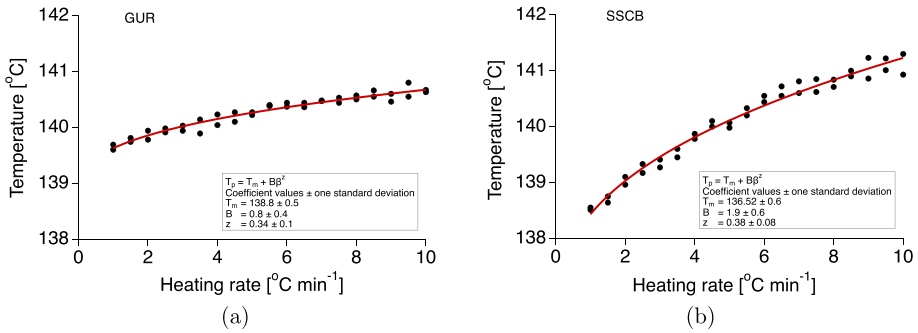

Fig. 3. Fitting of the melting peak temperature against heating rate with Equation (8) for the GUR (a) and SSCB (b) samples.

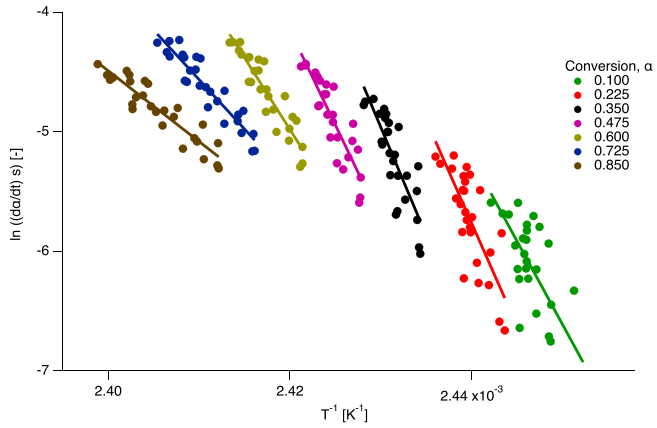

Fig. 4. A few representative Arrhenius plots used for the determination of E_α of the SSCB grade. Each color represent datapoints at the same extent of conversion collected from heating runs with a different heating rate. (For interpretation of the references to colour in this figure legend, the reader is referred to the web version of this article.)

$$\lambda_{max} = \frac{N_e L_0}{\sqrt{c_\infty N_e L_0^2}} \sim \sqrt{N_e} \sim \sqrt{M_e} \tag{8}$$

The ultra-drawability of the samples was investigated by the 2-stage drawing protocol described earlier. All samples were tested for possible melting by DSC after drawing, where the absence of the melt-crystallized, low temperature, melting peak (see Fig. 1) suggests that the samples are still nascent. The samples produced by the single-site catalytic systems (SSCA and SSCB) were already translucent after compression molding and could be easily calendered into translucent coherent films. On the contrary, the GUR and the ZNE grades were opaque after compression molding and calendering resulted in poorly coherent films, that for the case of GUR could not be drawn further. The maximum achieved draw ratio is reported in Table 2. The GUR and the ZNE grades show very poor drawability, the low entangled ZNLE is fairly drawable and the single-site catalyst (SSCA and SSCB) grades show excellent drawability.

3.2. Isoconversional analysis and apparent activation energy of melting

3.2.1. Apparent activation energy of melting of the different UHMWPE grades

It is well known that UHMWPE exhibits a high melting temperature of about 140 °C that is lost upon melt-crystallization and subsequent

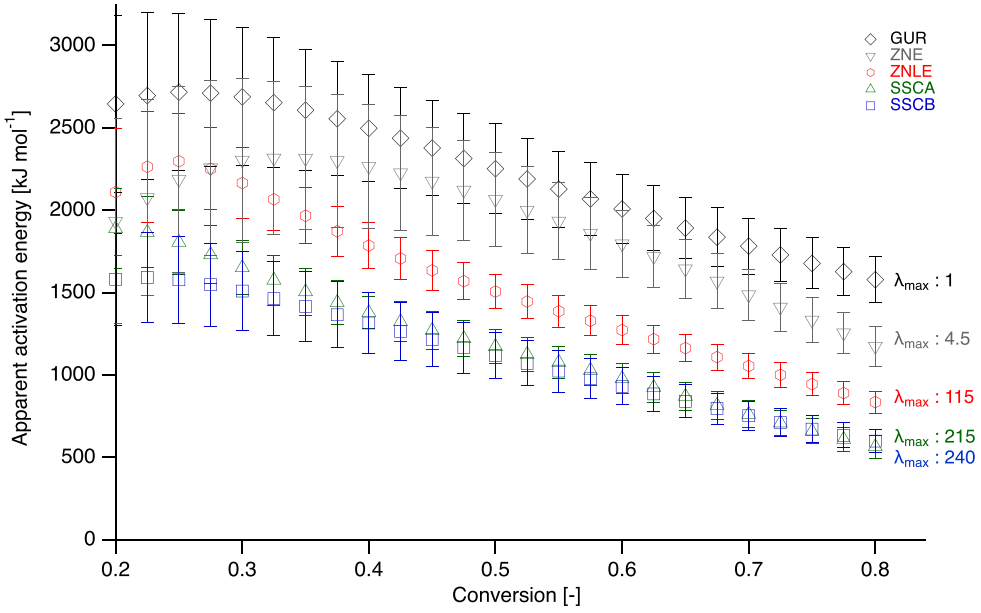

Fig. 5. Apparent activation energy as a function of conversion (loss of crystallinity during melting) of different nascent UHMWPE grades prepared via different catalytic systems. Black ⋄: GUR, grey ▽: ZNE, red: ZNLE, green △: SSCA, blue □: SSCB. (For interpretation of the references to colour in this figure legend, the reader is referred to the web version of this article.)

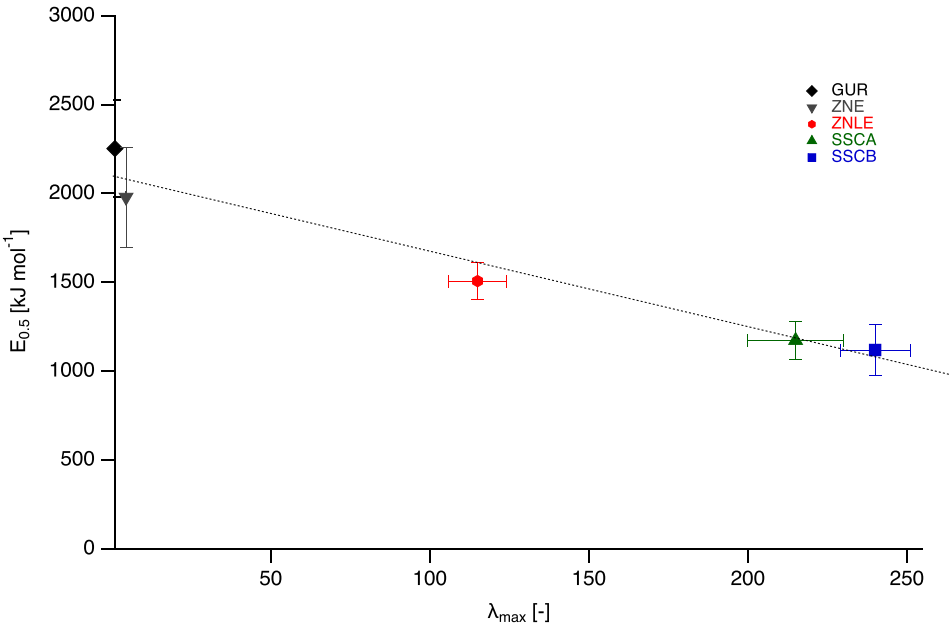

Fig. 6. Apparent activation energy values at a conversion of 0.5 against λ_{max} for the different UHMWPE grades. Black ⋄: GUR, grey ▽: ZNE, red: ZNLE, green △: SSCA, blue □: SSCB. The dashed line is a guide to the eye. (For interpretation of the references to colour in this figure legend, the reader is referred to the web version of this article.)

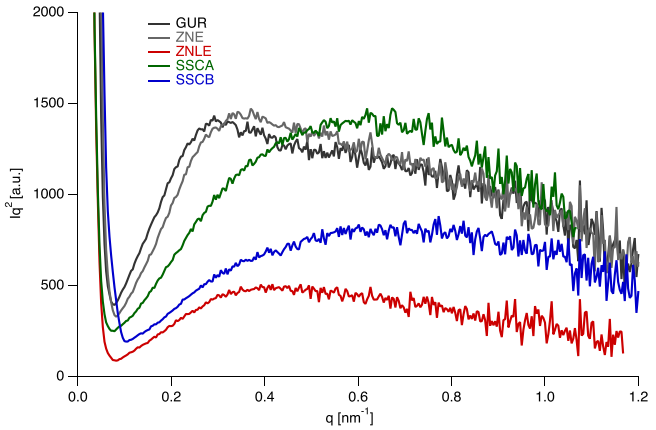

Fig. 7. Lorentz-corrected scattering intensities of the different nascent UHMWPE powders. Black: GUR, grey: ZNE, red: ZNLE, green: SSCA, blue: SSCB. (For interpretation of the references to colour in this figure legend, the reader is referred to the web version of this article.)

melting [19,48,49]. The high temperature melting peak and the high enthalpy of melting of nascent UHMWPE are clearly visible in the DSC curves of Fig. 1, where the initial (solid black lines) and subsequent (dotted blue lines) heating runs are presented. Fig. 1 depicts the commercial, entangled, GUR and the highly disentangled SSCB grades. Both entangled and disentangled nascent powders show this difference between nascent and melt-crystallized samples, in agreement with previous studies [19,20].

Fig. 2 demonstrates some DSC curves, at different heating rates and with the baseline subtracted, of the nascent SSCB powder, representative of our melting data. The increase of the melting temperature by increasing heating rate was utilized for the isoconversional analysis.

A way to check for superheating was suggested by Toda et al. [25], who examined the heating-rate dependence of the melting peak using Equation (9).

$$T_{p,\beta} = T_m + B\beta^z \tag{9}$$

Here, $T_{p,\beta}$ is the melting peak temperature for each heating rate, T_m the non-equilibrium melting temperature and B and z fitting parameters. The value of z corresponds to the heating rate dependance of the shift in peak temperature and if it is smaller than 0.5, melting can be regarded as kinetically controlled. The fitting was performed by having T_m, B and z as fit coefficients, as common methods to calculate T_m, like the Iller's equation, return unrealistic high values that are not consistent with the experimental observations, possibly due to the special nature of nascent UHMWPE crystals. From the fitting of T_p against β, a value smaller than 0.5 is obtained for parameter z, indicating kinetically controlled melting. Two representative graphs, namely for the GUR and SSCB samples, are presented in Fig. 3.

The E_α of melting was calculated for the different UHMWPE nascent powders. Some of the Arrhenius plots from which the E_α values of the SSCB grade were calculated are presented in Fig. 4. It should be noted that the plots presented in this figure correspond to just a fraction of the data analyzed for the E_α calculation.

The E_α dependence on conversion (α) for the different grades is presented in Fig. 5. The high values obtained are in accordance with previous reports on the melting of polymers [20,27,30].

The shape of the E_α is similar for all the grades analyzed and shows a decreasing dependance on conversion. In addition, there is almost no overlap of the curves of the different grades, especially at the regime with the higher confidence. For our comparisons we utilized the values of E_α at a conversion of 0.5 ($E_{0.5}$), since the relative error of the Arrhenius-type fitting is the smallest at this value. There seems to be a correlation between the level of disentanglement and the apparent activation energy, as the values of λ_{max} are increasing by decreasing values of $E_{0.5}$. This trend can be observed when the values of $E_{0.5}$ are plotted against the values of λ_{max}, as is presented in Fig. 6. This correlation is in agreement with the observation by Rastogi et al. [19] that the disentangled nascent UHMWPE melts faster than the entangled one. The lower value of the apparent activation energy calculated by our experiments for the more disentangled grades can explain this behavior. As melting of nascent UHMWPE is governed by kinetics, a lower activation energy of melting will translate into a faster melting. The calculation of the E_α could, therefore, possibly be used as an alternative way of evaluating the level of disentanglement of UHMWPE reactor powders.

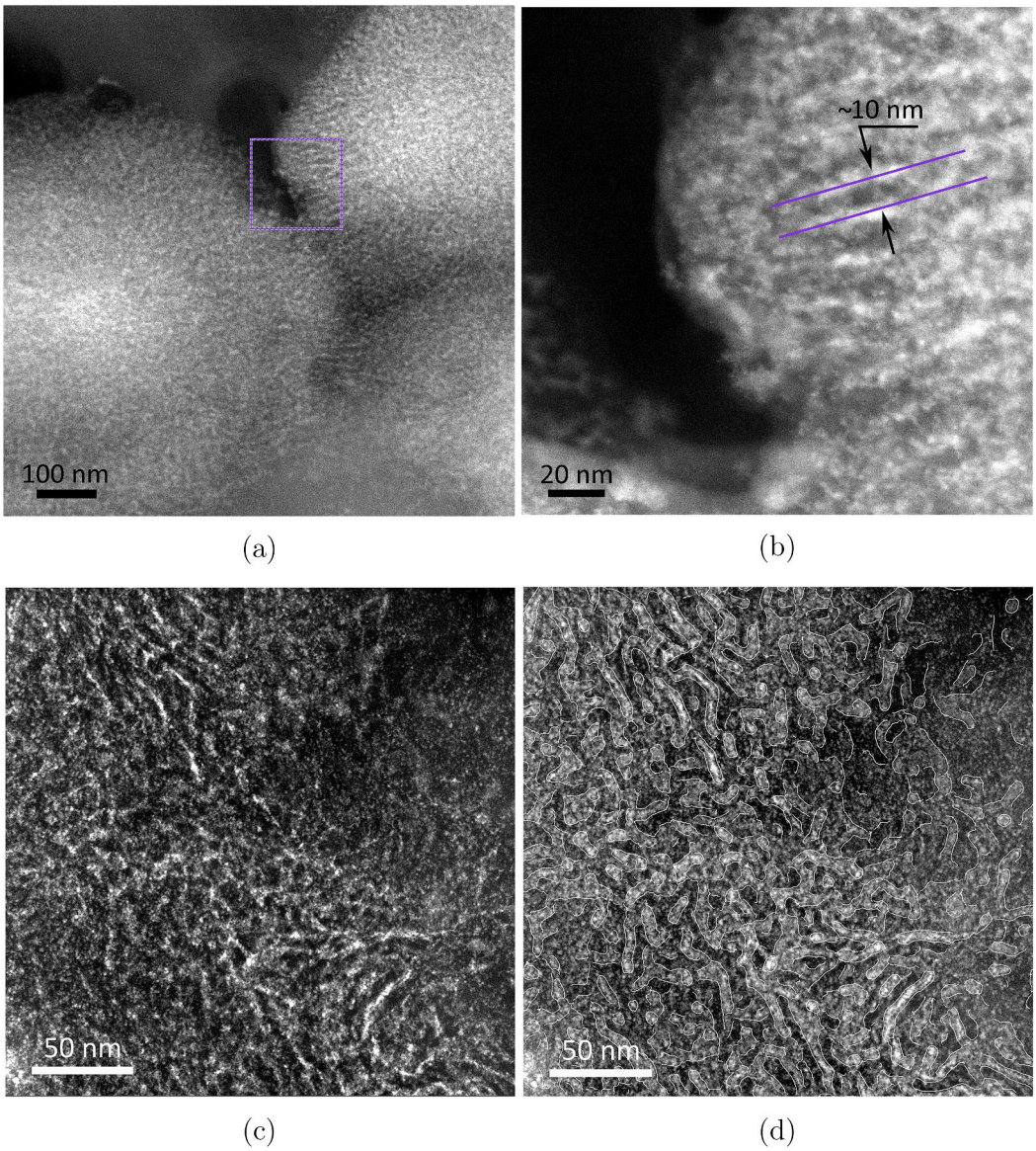

Fig. 8. STEM micrographs of the GUR (top) and SSCB (bottom) grades stained with ruthenium tetroxide at two different magnifications. The bright contrast in HAADF STEM micrographs corresponds to the Ru-rich regions. The micrograph (b) corresponds to the area framed in micrograph (a). Image (d) shows the micrograph of the SSCB grade (c) overlaid with the one where the edge-detect filter has been applied.

3.3. Microstructure analysis

In order to get an insight into the origin of the differences in the E_α, a microstructural aspect of the nascent powders, the lamellar thickness, was investigated. First, it was attempted to measure the long-period (L) through small-angle X-ray scattering. The samples were prepared according to the protocol described by Westfahl et al. in order to suppress the contribution from the grain-air interface of the nascent UHMWPE powder particles [42]. The crystallinity was measured by wide-angle X-ray scattering and the values obtained are presented in Table 2.

Unfortunately, as can bee seen from Fig. 7, the Lorentz-corrected SAXS intensity curves show only broad maxima, especially for the more disentangled samples. This could be related to a combination of factors, such as the irregular stacking of the lamellae [50], the small lateral dimensions, of especially the more disentangled samples, the uncertainty on how well the solvent is penetrating in all the pores of the powder or that a stronger X-ray source would be needed for such measurements. However, if the q-values, corresponding to the Lorentz-corrected intensity maxima of the curves of Fig. 7, are used for the calculation of an approximate value of the lamellar thickness, it can be seen that there is a trend of decreasing lamellar thickness with decreasing values of $E_{0.5}$. The estimated lamellar thickness values correspond to GUR: $\sim$ 13 nm, ZNE: $\sim$ 11 nm, ZNLE: $\sim$ 10.5 nm, SSCA: $\sim$ 7.2 nm and SSCB: $\sim$ 7 nm.

In order to confirm the trend identified from the SAXS measurements, direct measurements of the thicknesses were performed by STEM using an atomic-number (Z) sensitive imaging mode with a high-angle annular-dark field detector (HAADF STEM). The HAADF image contrast is proportional to Z^2 and is, therefore, especially suited for imaging the elemental-content modulations in a specimen. Ruthenium-tetroxide, containing heavy Ru atoms that produce a high contrast in HAADF STEM images, is used to stain the amorphous part of the UHMWPE, so the crystalline lamella would correspond to the unstained features of the micrographs. The successful staining was confirmed through energy-dispersive X-ray spectroscopy (EDS) element mapping. For the evaluation of the lamellar thicknesses, the HAADF micrographs of the stained specimens were used. An edge-detect filtering was applied to the micrographs and the filtered images were analyzed with the help

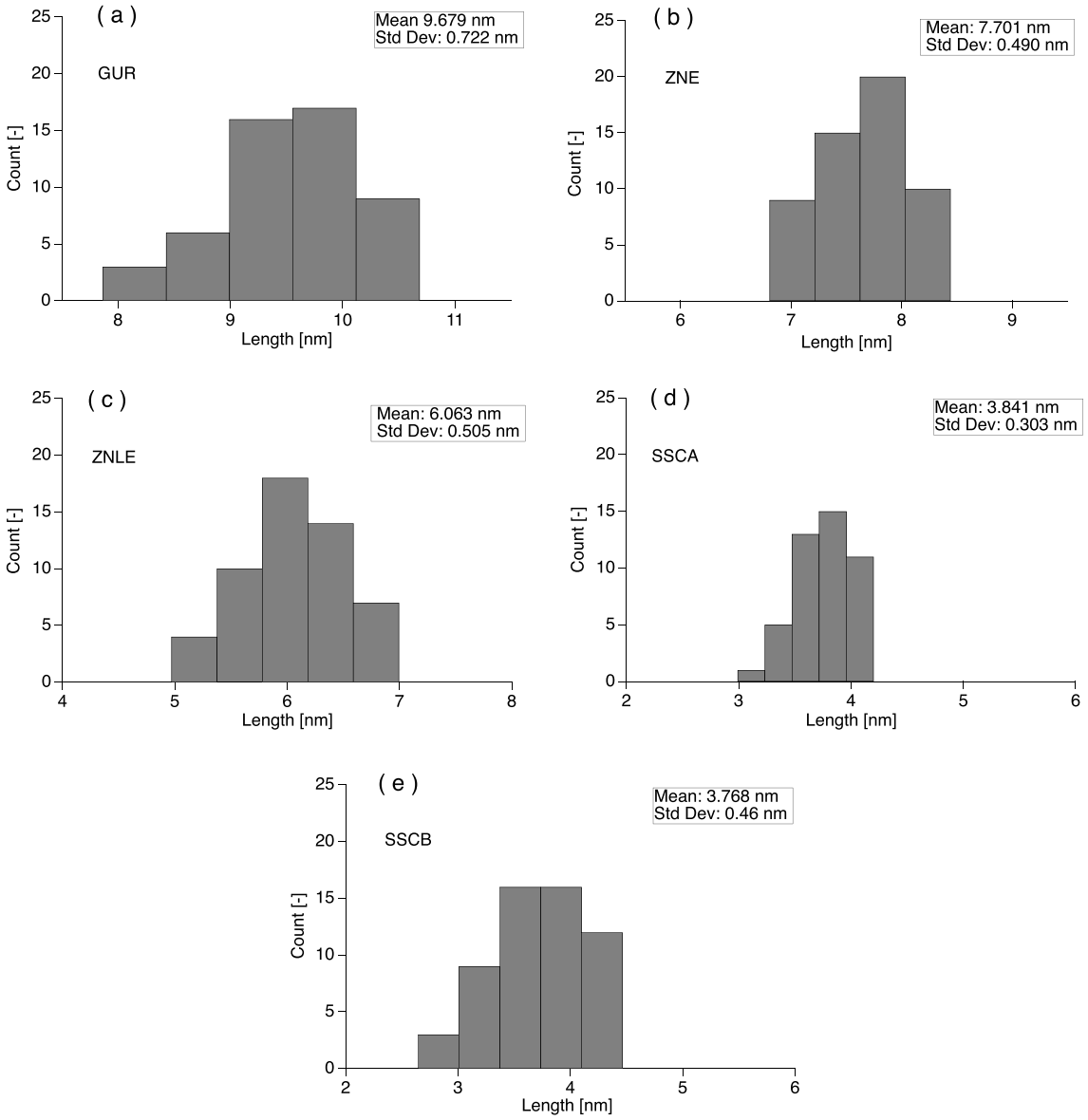

Fig. 9. Histograms of the lamellar thickness, as measured from the STEM micrographs, for the different UHMWPE grades: (a) GUR, (b) ZNE, (c) ZNLE, (d) SSCA, (e) SSCB.

of an ImageJ script. STEM micrographs, representative of our data, are presented in Fig. 8, where the original HAADF, filtered and superimposed images are shown. For the calculation of the lamellar thickness the distance between the amorphous part are measured and at least 50 measurements where conducted on ten different STEM micrographs for each grade. The distribution of the measured lamellar thickness is presented in Fig. 9 and the values included in Table 2. In addition, Fourier analysis of the STEM images was performed, as explained in Section 2.7, as an additional method to provide unbiased lamellar thickness values. The results for the lamellar thickness values obtained from the different evaluation methods are presented in Table 2 and are in very closed proximity to those measured earlier, and exhibit the same trend with respect to $E_{0.5}$.

Even though the determination of the exact value of the lamellar thickness is challenging, the obtained values are in agreement with the trend that was suggested by the SAXS measurements of the lamellar thickness.

Fig. 10 depicts the $E_{0.5}$ values as a function of lamellar thickness as measured by STEM, showing a clear trend of increasing lamellar thickness with increasing value of $E_{0.5}$. According to the kinetic theory of polymer melting [25], the apparent activation energy of melting E_α equals:

$$E_\alpha = -R\left[\frac{\partial \ln(\mathrm{d}\alpha/\mathrm{d}t)}{\partial T^{-1}}\right]_\alpha = A\left[\frac{1}{\Delta T} + \frac{2T}{(\Delta T)^2}\right] \tag{10}$$

Here, R is the universal gas constant, α is the extent of melting ("conversion"), which runs from 0 (fully crystalline) to 1 (fully molten), ΔT is the superheating and A is a constant:

$$A = \frac{\pi l \sigma^2 T_\mathrm{m}^0}{\Delta H_\mathrm{f}}, \tag{11}$$

where σ is the lateral-side interfacial free energy of a cylindrical nucleus, l is the lamellar thickness, T_m^0 is the equilibrium melting temperature and ΔH_f is the heat of fusion per unit volume. From Eqs. (10) and (11), assuming a constant σ, it follows that the apparent activation energy is expected to be proportional to the lamellar thickness l, which is in agreement with the correlation depicted in Fig. 6. Furthermore, from standard theory of polymer crystallization [51], it is well known that large undercooling leads to fast crystallization of polymer crystals with a

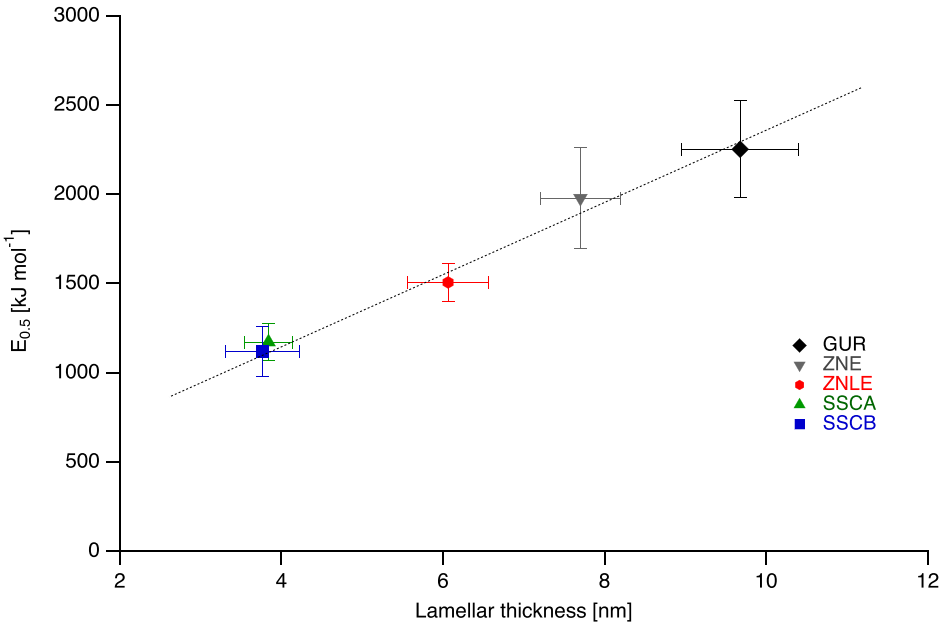

Fig. 10. Apparent activation energy at a conversion value of 0.5 against lamellar thickness as measured from the STEM micrographs. Black ⋄: GUR, grey ▽: ZNE, red: ZNLE, green △: SSCA, blue □: SSCB. The dashed line is a guide to the eye. (For interpretation of the references to colour in this figure legend, the reader is referred to the web version of this article.)

small lamellar thickness. For the synthesis of nascent UHMWPE, it is also known that fast cooling reduces the chance of the formation of entanglements of the growing macromolecular chain [12]. Using the correlation observed in Fig. 6, this would then agree with the observation that nascent UHMWPE powders that depict a small lamellar thickness (indicating a large undercooling) lead to films that show a large λ_{max} value (low entanglement density). Finally, it should be noted that the apparent activation energy for melting does not directly relate to the melting temperature as observed in a standard DSC experiment, as the full kinetic equation also includes the pre-exponentional factor and the detailed kinetic model [27]. In other words, a low activation energy can still result in a relative high melting point and the other way around.

4. Conclusions

The standard way of the production of high strength/high modulus UHMWPE fibers is the gel-spinning route. However, an alternative method, which avoids the use of excessive amounts of solvent, is solid-state processing of disentangled nascent UHMWPE reactor powder, followed by ultra drawing into high-performance polyethylene fibers or tapes. Here, as is the case in gel-spinning, the lower the entanglement density of the nascent powder, the better is the drawability, leading to superior fiber properties. In our work we use isoconversional analyses of DSC heating experiments up to melting to evaluate the apparent activation energy of melting. Moreover, we correlate the magnitude of the apparent activation energies, determined for all examined UHMWPE grades, to the level of disentanglement of each grade, as measured by solid-state drawability. It was found that the more disentangled materials exhibit a lower apparent activation energy, confirming earlier studies that the level of disentanglement of nascent UHMWPE is depicted in its melting kinetics. It is important to note that a high melting temperature of the nascent powder or the presence of superheating alone, is not necessarily indicative of disentangled material in itself, as both entangled and disentangled powders used in the present study depict superheating having a high initial melting temperature. To further investigate the reason behind the differences of the apparent activation energy of melting, the microstructure of these powders was determined, by measuring the lamellar thickness using SAXS experiments combined with STEM imaging. It was found that thinner lamella correspond to a lower apparent activation energy of melting, in agreement with current kinetic theories of polymer melting. In addition, thinner lamella are indicative of a faster crystallization during polymerization, which has been identified as one of the preferred conditions to obtain nascent UHMWPE reactor powder with a desired low entanglement density. This then explains the observed correlation between apparent activation energy of melting and maximum drawability, which could be used for identification of nascent UHMWPE powder grades to be used for high-performance polyethylene fibers and tapes.

Declaration of competing interest

The authors declare that they have no known competing financial interests or personal relationships that could have appeared to influence the work reported in this paper.

Acknowledgments

The authors thank ScopeM of ETH Zürich for use of the facilities for the specimen preparation and electron microscopy studies and Dr. André Brem for help with the isoconversional analysis. Authors are also grateful to Dr. Anne Greet Bittermann from ScopeM for helping with the specimen preparation and Dr. Thomas Webber for access to the X-ray Platform of the materials department of ETHZ. F.C. gratefully acknowledges funding by SABIC.

References

[1] W.E. Morton, J.W.S. Hearle, Physical Properties of Textile Fibres, CRC Press Woodhead Publishing, Cambridge, England, 2008.
[2] R. Hufenus, Y. Yan, M. Dauner, T. Kikutani, Melt-spun fibers for textile applications, Materials (Basel) 13 (19) (2020) 1–32, https://doi.org/10.3390/ma13194298.
[3] A. Ciferri, I.M. Ward (Eds.), Ultra-high Modulus Polymers, Applied Science Publishers, London, 1979.
[4] L. Balzano, B. Coussens, T. Engels, F. Oosterlinck, M. Vlasblom, H. van der Werff, D. Lellinger, Multiscale structure and microscopic deformation mechanisms of gel-spun ultrahigh-molecular-weight polyethylene fibers, Macromolecules 52 (14) (2019) 5207–5216, https://doi.org/10.1021/acs.macromol.9b00247.
[5] Y. Rao, A. Waddon, R. Farris, Structure-property relation in poly(p-phenylene terephthalamide) (PPTA) fibers, Polymer 42 (13) (2001) 5937–5946, https://doi.org/10.1016/S0032-3861(00)00905-8.

[6] J.W.S. Hearle, High-performance Fibres, CRC Press Woodhead Pub, Cambridge, England, 2001.

[7] P. Smith, P.J. Lemstra, Ultra-high-strength polyethylene filaments by solution spinning/drawing, J. Mater. Sci. 15 (1980) 505–514, https://doi.org/10.1016/0032-3861(80)90205-0.

[8] P. Smith, P.J. Lemstra, H.C. Booij, Ultradrawing of high-molecular-weight polyethylene cast from solution. II. Influence of initial polymer concentration, J. Polym. Sci. Polym. Phys. Ed 19 (5) (1981) 877–888, https://doi.org/10.1002/pol.1981.180190514.

[9] A. Brem, O. Lhost, T.A. Tervoort, Influence of solvent quality and crystallization conditions on the drawability of ultra-high molecular weight polyethylene cast from solution, Macromolecules 53 (14) (2020) 5957–5970, https://doi.org/10.1021/acs.macromol.0c00756.

[10] P. Smith, P.J. Lemstra, Ultra-high strength polyethylene filaments by solution spinning/drawing. 3. Influence of drawing temperature, Polymer 21 (1980) 1341–1343, https://doi.org/10.1016/b978-0-12-802650-2.00006-6.

[11] R. Schaller, K. Feldman, P. Smith, T.A. Tervoort, High-performance polyethylene fibers “Al Dente”: improved gel-spinning of ultrahigh molecular weight polyethylene using vegetable oils, Macromolecules 48 (24) (2015) 8877–8884, https://doi.org/10.1021/acs.macromol.5b02211.

[12] P. Smith, H.D. Chanzy, B.P. Rotzinger, Drawing of virgin ultrahigh molecular-weight polyethylene - an alternative route to high-strength fibers, Polym. Commun. 26 (9) (1985) 258–260.

[13] P. Smith, H.D. Chanzy, B.P. Rotzinger, Drawing of virgin ultrahigh molecular weight polyethylene: an alternative route to high strength/high modulus materials - Part 2 Influence of polymerization temperature, J. Mater. Sci. 22 (2) (1987) 523–531, https://doi.org/10.1007/BF01160764.

[14] B.P. Rotzinger, H.D. Chanzy, P. Smith, High strength/high modulus polyethylene: synthesis and processing of ultra-high molecular weight virgin powders, Polymer 30 (10) (1989) 1814–1819, https://doi.org/10.1016/0032-3861(89)90350-9.

[15] P. Smith, P.J. Lemstra, H. Booij, Ultradrawing of high-molecular-weight polyethylene cast from solution. II influence of initial polymer concentration, J. Polym. Sci. 19 (1981) 877–888.

[16] K. Kawai, T. Fujita, Discovery and development of FI catalysts for olefin polymerization: unique catalysis and distinctive polymer formation, Top. Organomet. Chem. 26 (10) (2009) 3–46, https://doi.org/10.1007/978-3-540-87751-6_1.

[17] T. Matsugi, T. Fujita, High-performance olefin polymerization catalysts discovered on the basis of a new catalyst design concept, Chem. Soc. Rev. 37 (6) (2008) 1264–1277, https://doi.org/10.1039/b708843b.

[18] S. Rastogi, Y. Yao, S. Ronca, J. Bos, J. Van Der Eem, Unprecedented high-modulus high-strength tapes and films of ultrahigh molecular weight polyethylene via solvent-free route, Macromolecules 44 (14) (2011) 5558–5568, https://doi.org/10.1021/ma200667m.

[19] S. Rastogi, D.R. Lippits, G.W.M. Peters, R. Graf, Y. Yao, H.W. Spiess, Heterogeneity in polymer melts from melting of polymer crystals, Nat. Mater. 4 (2005) 635–641, https://doi.org/10.1038/nmat1437.

[20] D.R. Lippits, S. Rastogi, G.W. Höhne, Melting kinetics in polymers, Phys. Rev. Lett. 96 (21) (2006) 2–5, https://doi.org/10.1103/PhysRevLett.96.218303.

[21] A. Pandey, A. Toda, S. Rastogi, Influence of amorphous component on melting of semicrystalline polymers, Macromolecules 44 (20) (2011) 8042–8055, https://doi.org/10.1021/ma201797k.

[22] D. Romano, N. Tops, E. Andablo-Reyes, S. Ronca, S. Rastogi, Influence of polymerization conditions on melting kinetics of low entangled uhmwpe and its implications on mechanical properties, Macromolecules 47 (14) (2014) 4750–4760, https://doi.org/10.1021/ma5008122.

[23] S. Vyazovkin, A.K. Burnham, J.M. Criado, L.A. Pérez-Maqueda, C. Popescu, N. Sbirrazzuoli, ICTAC Kinetics Committee recommendations for performing kinetic computations on thermal analysis data, Thermochim. Acta 520 (1–2) (2011) 1–19, https://doi.org/10.1016/j.tca.2011.03.034.

[24] S. Vyazovkin, Isoconversional Kinetics of Thermally Stimulated Processes, Springer, 2015, https://doi.org/10.1007/978-3-319-14175-6.

[25] A. Toda, M. Hikosaka, K. Yamada, Superheating of the melting kinetics in polymer crystals: a possible nucleation mechanism, Polymer 43 (5) (2002) 1667–1679, https://doi.org/10.1016/S0032-3861(01)00733-9.

[26] A. Toda, I. Kojima, M. Hikosaka, Melting kinetics of polymer crystals with an entropic barrier, Macromolecules 41 (1) (2008) 120–127, https://doi.org/10.1021/ma702162m.

[27] F. Christakopoulos, E. Troisi, T.A. Tervoort, Melting kinetics of nascent poly (tetrafluoroethylene) powder, Polymers 12 (4) (2020) 791, https://doi.org/10.3390/polym12040791.

[28] S. Vyazovkin, Isoconversional kinetics of polymers: the decade past, Macromol. Rapid Commun. 38 (3) (2017) 1–21, https://doi.org/10.1002/marc.201600615.

[29] S. Vyazovkin, N. Sbirrazzuoli, Isoconversional kinetic analysis of thermally stimulated processes in polymers, Macromol. Rapid Commun. 27 (18) (2006) 1515–1532, https://doi.org/10.1002/marc.200600404.

[30] S. Vyazovkin, B. Yancey, K. Walker, Nucleation-driven kinetics of poly (ethylene terephthalate) melting, Macromol. Chem. Phys. (2013) 2562–2566.

[31] A. Toda, K. Taguchi, K. Nozaki, T. Fukushima, H. Kaji, Superheated melting kinetics of metastable chain-folded polymer crystals, Cryst. Growth Des. 18 (6) (2018) 3637–3643, https://doi.org/10.1021/acs.cgd.8b00416.

[32] A. Toda, K. Taguchi, K. Nozaki, Fast limiting behavior of the melting kinetics of polyethylene crystals examined by fast-scan calorimetry, Thermochim. Acta 677 (November 2018) (2018) 211–216, https://doi.org/10.1016/j.tca.2018.12.024.

[33] J. Menczel, R. Prime, Thermal Analysis of Polymers: Fundamentals and Applications, John Wiley and Sons, 2008, https://doi.org/10.1002/9780470423837.

[34] B. Wunderlich, C.M. Cormier, Heat fusion polyethylene, J. Polym. Sci. 2 Polym. Phys. 5 (1967) 987–988.

[35] H.E. Kissinger, Reaction kinetics in differential thermal analysis, Anal. Chem. 29 (11) (1957) 1702–1706, https://doi.org/10.1021/ac60131a045.

[36] H.L. Friedman, Kinetics of thermal degradation of char-forming plastics from thermogravimetry. Application to a phenolic plastic, J. Polym. Sci. Part C: Polymer Symposia 6 (1) (1964) 183–195, https://doi.org/10.1002/polc.5070060121.

[37] S. Vyazovkin, A unified approach to nonisothermal data, Unified Kinetic Processing 28 (2) (1995) 95–101.

[38] S. Vyazovkin, C.A. Wight, Isothermal and non-isothermal kinetics of thermally stimulated reactions of solids, Int. Rev. Phys. Chem. 17 (3) (1998) 407–433, https://doi.org/10.1080/014423598230108.

[39] S. Arrhenius, Über die Reaktionsgeschwindigkeit bei der Inversion von Rohrzucker durch Säuren, Z. Phys. Chem. 4U (1). doi:10.1515/zpch-1889-0416.

[40] W. Ruland, X-ray determination of crystallinity and diffuse disorder scattering, Acta Crystallogr. 14 (11) (1961) 1180–1185, https://doi.org/10.1107/s0365110x61003429.

[41] Z. Mo, H. Zhang, The degree of crystallinity in polymers by wide-angle X-ray diffraction (WAXD), J. Macromol. Sci., Part C 35 (4) (1995) 555–580, https://doi.org/10.1080/15321799508021751.

[42] H. Westfahl, M.B. Cardoso, Accessing the hidden lamellar nanostructure of semi-crystalline nascent polymers by small-angle X-ray scattering contrast variation, J. Appl. Crystallogr. 44 (5) (2011) 1123–1126, https://doi.org/10.1107/S0021889811033255.

[43] C.G. Vonk, Investigation of non-ideal two-phase polymer structures by small-angle X-ray scattering, J. Appl. Crystallogr. 6 (2) (1973) 81–86, https://doi.org/10.1107/s0021889873008204.

[44] A.J. Ryan, W. Bras, G.R. Mant, G.E. Derbyshire, A direct method to determine the degree of crystallinity and lamellar thickness of polymers: application to polyethylene, Polymer 35 (21) (1994) 4537–4544, https://doi.org/10.1016/0032-3861(94)90799-4.

[45] W. Pratt, Digital Image Processing: PIKS Scientific inside, John Wiley & Sons, 2007, https://doi.org/10.1007/978-94-009-7163-9_6.

[46] Helmut Gruender site directory, http:www.gluender.de/home/home.html, [Online; accessed 4-January-2021].

[47] Radial profile extended, http:www.questpharma.u-strasbg.fr/html/radial-profile-ext.html, [Online; accessed 4-January-2021].

[48] X. Wang, R. Salovey, Melting of ultrahigh molecular weight polyethylene, J. Appl. Polym. Sci. 34 (2) (1987) 593–599, https://doi.org/10.1002/app.1987.070340214.

[49] R.A. Phillips, Morphology and melting behavior of nascent ultra-high molecular weight polyethylene, J. Polym. Sci. B Polym. Phys. 36 (3) (1998) 495–517.

[50] Y.M.T. Tervoort-Engelen, P.J. Lemstra, Morphology of nascent ultra-high molecular weight polyethylene reactor powder: chain-extended versus chain-folded crystals, Polym. Commun. 32 (11) (1991) 343–345.

[51] J.I. Lauritzen, J.D. Hoffman, Formation of polymer crystals with folded chains from dilute solution, J. Chem. Phys. 31 (6) (1959) 1680–1681, https://doi.org/10.1063/1.1730678.